Enhanced pool boiling heat transfer using novel inverted trapezoid microgroove structures

M Muneeshwaran*, Jamieson Brechtl, Kashif Nawaz, Cheng-Min Yang*

Building Technologies Research and Integration Center, Oak Ridge National Laboratory, Oak Ridge - 37831, Tennessee, USA

*Corresponding authors: muruganm@ornl.gov; yangc1@ornl.gov

Abstract

Pool boiling heat transfer improvements with enhanced surfaces have been extensively studied for various hydrofluorocarbon (HFC) refrigerants. However, there is a limited number of studies in the open literature that focus on the pool boiling heat transfer characteristics of hydrofluoroolefin (HFO) refrigerants on enhanced surfaces. This study aims to address this gap by analyzing the pool boiling behavior of HFO refrigerants, specifically R1234yf and R1234ze(E). Experiments were conducted on both plain surfaces and novel inverted trapezoid microgroove structures. The experimental results indicate that the microgroove structures can improve heat transfer coefficients by up to 80% compared to plain surfaces. Additionally, the performance of R1234yf and R1234ze(E) was compared to that of R134. It was observed that R1234yf exhibited comparable performance to R134a, while R1234ze(E) showed slightly lower performance. To assess the influence of saturation temperature on pool boiling heat transfer, tests were conducted at different saturation temperatures of 15℃, 25℃, and 35℃. The findings revealed that the pool boiling heat transfer coefficient increases with rising saturation temperature.

Keywords: Pool boiling; HFO refrigerants; microgroove; heat transfer coefficient

Introduction

Pool boiling heat transfer is a crucial heat transfer mechanism in refrigeration and air-conditioning equipment, such as flooded evaporators. The pool boiling heat transfer can be augmented by having more nucleation sites on the boiling surface, which has been achieved through several ways including surface area enhancement (finned, wicked, and porous surfaces) and surface roughness enhancement. And it has been extensively studied for various hydrofluorocarbon (HFC) refrigerants on both smooth and enhanced surfaces, such as R134a , R32 , R125 , R143a , and R410A [1]. For example, Dewangan et al. [2] investigated the pool boiling behavior on a plain

surface using R134a and R410A refrigerants. They conducted experiments at saturation temperatures of 5°C, 10°C, 15°C, and 20°C, with a heat flux range of 10–70 kW m^{-2}. Their results indicated that the heat transfer coefficients (HTC) of R134a were 20–39% lower than those of R410A. Similarly, Hsu et al. [3] compared the pool boiling performance of R32 with R410A on a smooth surface, finding that R32 HTCs are slightly higher than those of R410A. Additionally, Li et al. [4], Jung et al. [5], and Koster et al. [6] examined the nucleate boiling characteristics of R32 and R143a on a smooth surface, respectively.

Smooth surfaces typically exhibit limited nucleate boiling heat transfer performance due to their smaller surface area and insufficient nucleation sites. To address this issue, several enhanced surfaces have been developed to improve pool boiling HTCs. Ribatski and Thome [7] conducted a series of experiments on various enhanced surfaces, including Gewa-B, Turbo-BII HP, Turbo-CSL, and High-Flux surfaces, using R134a refrigerant. The Gewa-B, Turbo-BII HP, Turbo-CSL, and High-Flux surfaces demonstrated enhancements in heat transfer by factors of 2.4–5.2, 1.8–7, 2.4–2.9, and 4.9–21.3, respectively, compared to a plain surface. Additionally, Dewangan et al. [8] compared the nucleate boiling performance of smooth surfaces with porous surfaces using R134a and R410A refrigerants. Their study found that porous surfaces can achieve 1.25–2 times higher HTCs than plain surfaces. Saidi et al. [9] analyzed the performance of two rough-finned surfaces using R123 refrigerant. These rough-finned surfaces demonstrated an improvement of nearly 130–240% compared to smooth surfaces. Hsieh and Ke [10] evaluated the performance of two plasma-coated surfaces (copper and molybdenum) under pool boiling conditions using R134a refrigerant. Their findings indicated that plasma-coated surfaces achieved higher HTCs than plain surfaces. In summary, various enhanced boiling surfaces have been developed to augment nucleate boiling HTCs, offering superior performance due to increased surface area and a greater number of nucleation sites.

The above summary makes it evident that the pool boiling characteristics of HFCs on both plain and enhanced surfaces have been extensively studied, with substantial data available in the open literature. In contrast, the boiling heat transfer characteristics of next generation refrigerants, particularly hydrofluoroolefin (HFO) refrigerants, such as R1234yf, R1234ze(E), R1233zd(E), R1336mzz(Z) , and R514A [1], have been investigated for only a limited number of enhanced

surfaces. Research on various enhanced surfaces for HFO refrigerants is still scarce, and only a few nucleate boiling heat transfer data points are available in the open literature.

Kedzierski and Lin [11] analyzed the performance of a flattened Turbo-ESP surface using R514A and R1336mzz(E), refrigerants expected to replace R123 and R245fa. They found that the performance of R514A and R1336mzz(E) was nearly 30% and 13% better than that of R123 within a heat flux range of 10–80 kW m^{-2}. In a similar study, Kedzierski and Lin [12] tested the characteristics of R1336mzz(Z) on the flattened Turbo-ESP surface at different saturation temperatures of 4.5°C, 25°C, and 45°C. The performance of R1336mzz(Z) was found to be superior at a saturation temperature of 25°C compared to 4.5°C and 45°C. Analogously, Kedzierski et al. [13] compared the performance of R134a with its potential replacements, such as R1234yf, R513A, and R450A, using the same flattened Turbo-ESP surface. The results indicated that the performance of R134a was nearly 16%, 19%, and 57% better than that of R1234yf, R513A, and R450A, respectively. Gorgy [14] tested the performance of R1234ze, R450A, and R1233zd(E) on an enhanced surface. Although the specific details of the enhanced tubes were not provided in Gorgy [14], Lin and Kedzerski [15] later categorized the enhanced surface used in Gorgy [14] as Turbo-ESP. According to Gorgy [14], the performance of R1234ze and R450A was similar but 28% lower than that of R134a, while R1233zd(E) showed a 19% improvement compared to R123. Lee et al. [16] analyzed three different flattened enhanced surfaces, including Tubo-B, Turbo-C, and Thermoexcel-E, using R1234yf. Their results suggested that the performance of R1234yf was comparable to that of R134a for all three surfaces. Similarly, Rooyen and Thome [17] investigated the performance of R1234ze(E) on Turbo-B5 and Gewa-B5 surfaces and found a similar performance between R1234ze(E) and R134a on both surfaces. Park and Jung [18] observed that the HTCs of R1234yf on a flattened low-fin surface were comparable to those of R134a. Nagata et al. [19] investigated the performance of three enhanced surfaces with different open-mouth widths using R1234ze(Z). These enhanced surfaces provided a 2.8–5.1-fold increase in HTC compared to plain tubes. Byun et al. [20] tested two enhanced surfaces with R1234ze(E) and R1233zd(E), finding that the HTCs of R1234ze(E) and R1233zd(E) were up to 18% and 75% lower than those of R134a on the enhanced surfaces.

Table 1: List of pool boiling studies related to R1234yf and R1234ze(E) with finned surfaces.

Author (Ref.)	Refrigerants	Enhanced Surface Features	Saturation Temperature [°C]	Surface Image
Park and Jung [18]	R1234yf	Low fins (Fin height = 1.21 mm)	7.0	NA
Lee et al. [16]	R1234yf	Turbo-B (Fin height = 0.44 mm; Gap = 0.085 mm), Turbo-C (Fin height = 0.76 mm; Gap = 0.35 mm), Thermoexcel-E (Fin height = 0.49 mm; Gap = 0.121 mm)	7.0	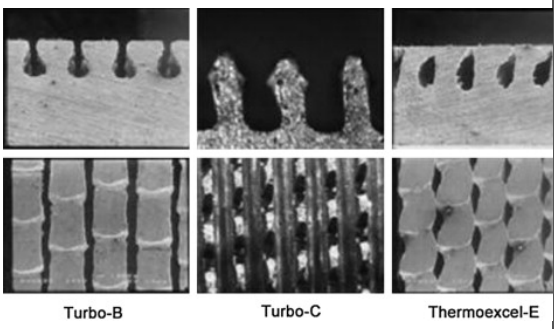
Kedzierski et al. [12, 21]	R1234yf; R1336mzz(Z)	Turbo-ESP (Fin height = 0.4 mm; Fin thickness = 0.2 mm; Gap = 0.04 mm; Fin slot width = 0.05 mm	4.5 – 45.0	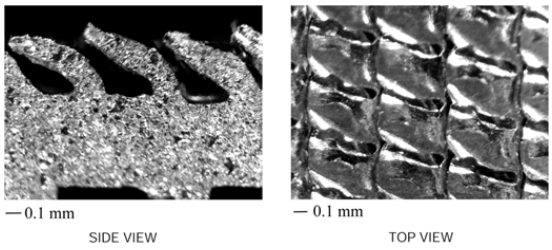
Lee et al. [22]	R1234yf	Low-fin (Fin height = 1.21 mm; Gap = 0.58 mm) Turbo-B (Fin height = 0.44 mm; Gap = 0.085 mm), Turbo-C (Fin height = 0.76 mm; Gap = 0.35 mm), Thermoexcel-E (Fin height = 0.49 mm; Gap = 0.121 mm)	7.0	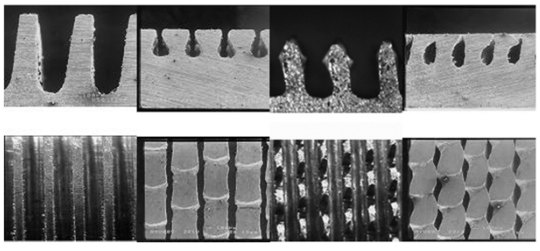 Fig. 2 Side and top views of enhanced surfaces.
Van Rooyen	R1234ze(E)	Turbo-B5, GEWA-B5	5.0 – 25.0	NA

and Thome [23]				
Byun et al. [20]	R1234ze(E)	Enhanced tube #1 (similar to Turbo-B, Fin height = 0.55 mm; Groove height = 0.35 mm); Enhanced tube #2 (similar to Turbo-BII, Fin height = 0.61 mm; Groove height = 0.34 mm)	4.4, 26.7	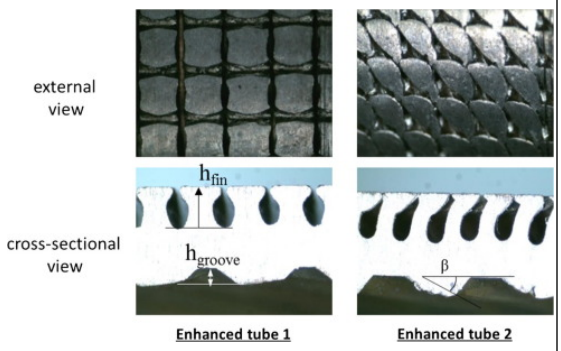
Kumar and Wang [24]	R1234ze(E)	GEWA-B5H (Fin height = 1.1 mm; Gap = 0.11–0.15 mm)	-6.0, 0, 10.0	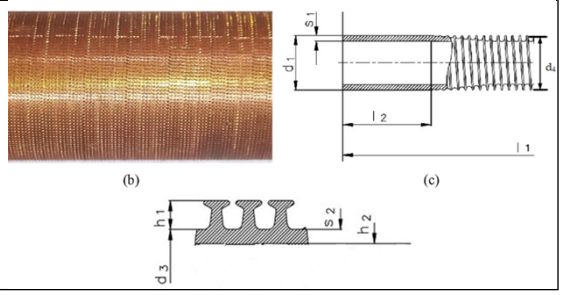

Table 1 summarizes the different pool boiling studies with enhanced surfaces using R1234yf and R1234ze(E) refrigerants (potential replacement for R134a). It is understood from Table 1 that the studies related to predicting the performance of enhanced surfaces with R1234yf and R1234ze(E) refrigerants are limited in the open literature. Moreover, the number of enhanced surfaces (e.g., finned surfaces) tested with these refrigerants are scarce in the open literature. Notably, most existing studies on these refrigerants have focused on “bent fin” and “reentrant cavity” type enhanced surfaces. However, according to the best of the authors knowledge, there are no studies available in the open literature concerning open microgroove geometries for both R1234yf and R1234ze(E) refrigerants. Therefore, this study aims to investigate the performance of a novel inverted trapezoid microgroove structure with R1234yf and R1234ze(E) refrigerants. The pool boiling performance of R1234yf and R1234ze(E) is tested at different heat fluxes and saturation temperatures, with the results compared against R134a.

2. Experimental setup and methodology

Fig. 1 shows the experimental setup for refrigerant pool boiling. The primary components of the system include an external condenser (i.e., plate heat exchanger), a chiller loop, a high-pressure stainless-steel vessel, a pool boiling test section, and a data acquisition system. The chamber wall was heated using an 800W grounded fiberglass-insulated electrical resistance tape heater (BriskHeat CPBIH101016LGT) wrapped around the vessel's outer surface. A digital PID temperature controller (BriskHeat SDXRA-THRN10-HA) was employed to regulate the wall temperature, and the pressure vessel was fully insulated to minimize heat loss to the surrounding environment. The tape heater is chosen for its flexibility, allowing it to wrap around the pressure vessel and provide uniform heating around the vessel. The primary purpose of the tape heater is to heat the pressure vessel to maintain a required saturation temperature, particularly when the saturation temperature exceeds the ambient temperature. Viewing windows on the pressure vessel allowed observation and recording of the boiling process during the experiment. Cooling water, supplied by a 15-kW recirculating chiller (Thermo Scientific, ThermoFlex 15000), was used to condense the vapor refrigerant back into the liquid phase in the external condenser during the experiment. The cooling water temperature was controlled through the chiller, and the water flow rate was regulated via a control valve to maintain the desired saturation pressure and temperature of the refrigerant in the pressure vessel. The vessel pressure was measured using an absolute pressure transducer (Omega PX409-500AI). Two T-type thermocouple probes (Omega TMQSS-062U) measured the refrigerant temperatures at the bottom and top of the vessel. All data were recorded using a National Instruments data acquisition system (NI cDAQ-9178) and visualized through a LabVIEW program.

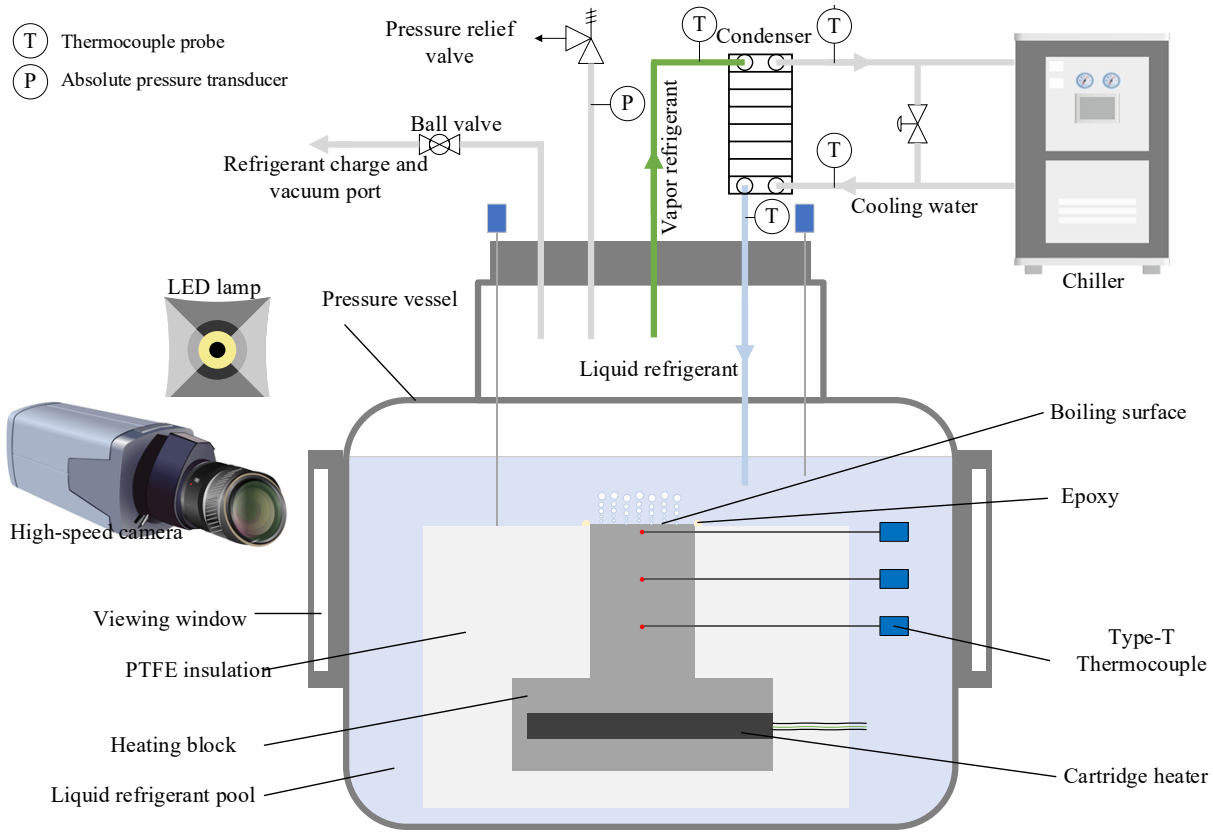

Fig. 1. Schematic of the experimental setup.

Fig. 2 (a) features the heat transfer test section, which is an inverted T-shaped aluminum alloy (6061) heating block. The heating block was designed to supply heat to the boiling surface and quantify the heat flux. The top surface (2.54 × 2.54 cm^2) of the heating block served as the boiling surface, and the newly developed microgroove geometry was directly machined on top of the heating block to avoid contact resistance. To ensure that the heat generated by the heaters was transferred to the top surface, the PTFE insulation was provided around the heating block, as shown in Fig. 2 (a). The thermal conductivity of PTFE insulation is approximately 0.3 W m^{-1} K^{-1}. Due to its lower thermal conductivity, the PTFE insulation significantly minimizes heat loss from the heating block. Additionally, as shown in Fig. 2 (b), three thermocouples are placed in each row to monitor the transverse heat conduction within the block. The temperature difference between the three thermocouples in each row was observed to be less than ±0.3°C, which is well within the thermocouple's uncertainty, indicating that heat loss from the heating block is negligible. The tiny gap between the insulation and the four sides of the tested surface was sealed using epoxy. Two 150W cartridge heaters (Watlow 2309-6594) were installed in reamed wells at the bottom of the

heating block to provide the necessary heat. An SCR controller (Watlow DB20-24F0-0000) was used to control the heating power of the test section during the experiment, and the power supplied to the cartridge heaters was measured through a watt transducer (Ohio Semitronics, PC5-107X5Y25) with a measurement range of 0 - 500 W. To measure the temperature gradient (and determine the heat flux) in the heating block, nine T-type thermocouples (Omega TMQSS-040U) were inserted in a 3 × 3 array, as shown in Fig. 2(b). The thermocouples were positioned at vertical intervals of 10 mm. All the thermocouples were calibrated against a NIST-traceable high-precision thermometer, with calibrated uncertainties of less than ±0.2°C. The accuracy details of the measurement instruments are presented in Table 2.

Table 2: Accuracy and model details of the instrument.

Parameters	**Instrument**	**Model**	**Range**	**Accuracy**
Pressure	Absolute pressure transducer	Omega PX409-500AI	0 - 500 psi	0.5% F.S.
Liquid pool temperature	T-type thermocouple	Omega TMQSS-062U	-250 to +350℃	±0.2℃
Heating block temperature	T-type thermocouple	Omega TMQSS-040U	-250 to +350℃	±0.2℃
Power	Watt Transducer	Ohio Semitronics, PC5-107X5Y25	0 - 500 W	±0.5% F.S.
Microgroove dimension	3D laser scanning confocal microscope	Keyence – VK-X3050	NA	0.40%
Roughness	Surface profilometer	Mitutoyo SJ-210	NA	±0.02 µm

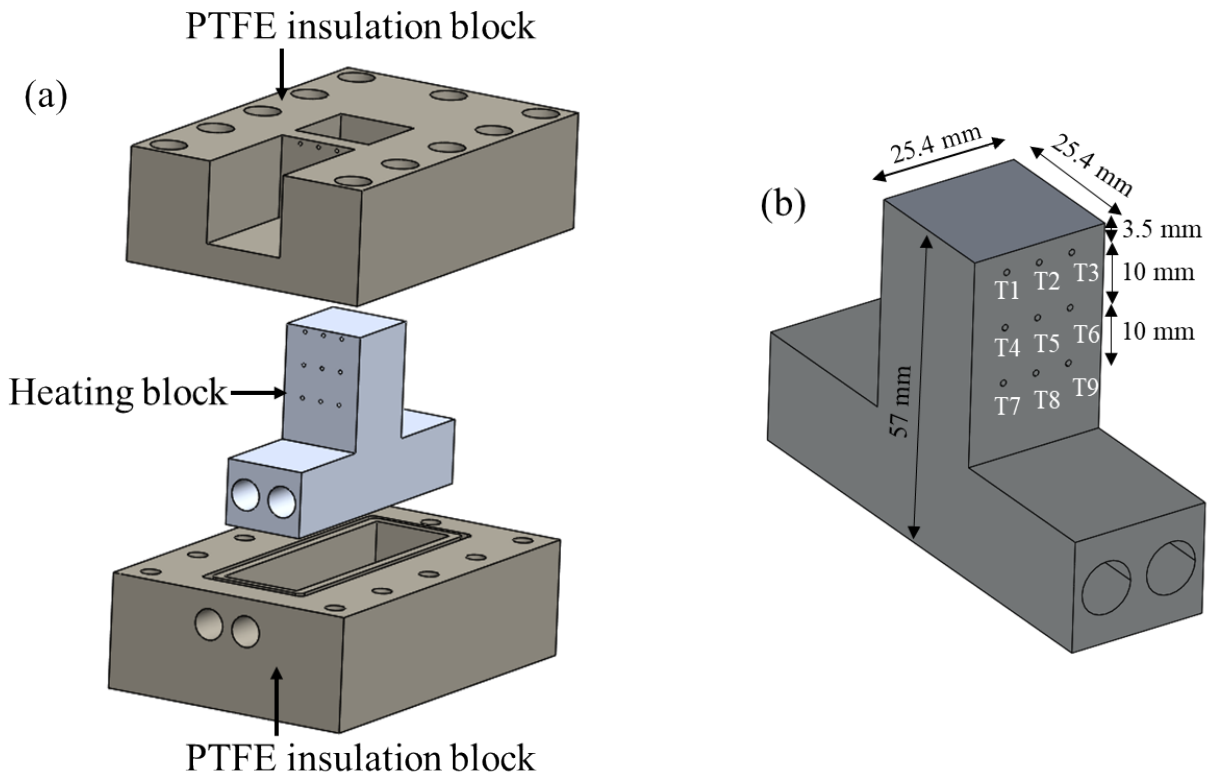

Fig. 2. (a) Assembly of the test section with heating block and PTFE insulation and (b) dimension details of the heating block.

For the pool boiling experiments in this study, one smooth surface and two types of inverted trapezoid microgroove-enhanced surfaces were investigated. The microgroove structure was directly machined on the top of the heating block through an end milling process on a CNC machine. The surface topography and a microscopic view of the enhanced surfaces were acquired using a 3D laser scanning confocal microscope (Keyence – VK-X3050), as illustrated in Fig. 3. The profile of these enhanced surfaces was also captured and presented in Fig. 3. The microgroove dimensions shown in Fig. 3 were measured using a 3D laser scanning confocal microscope. This profilometer is calibrated to an accuracy of less than 0.4%, ensuring a level of precision that is significantly higher than conventional methods. The detailed dimensions of the microgroove geometries are provided in Table. 3. The microgroove structure with a groove height of 132 µm and groove width of 126 µm and 64 µm at the top and base, respectively, is hereafter referred to as enhanced surface 1. Similarly, the microgroove structure with height of 160 µm and groove width of 116 µm and 67 µm at the top and base, respectively, is hereafter referred to as enhanced

surface 2. The roughness of the plain surface was measured using a profilometer (Mitutoyo SJ-210) and it was measured to be 1.052±0.25 µm.

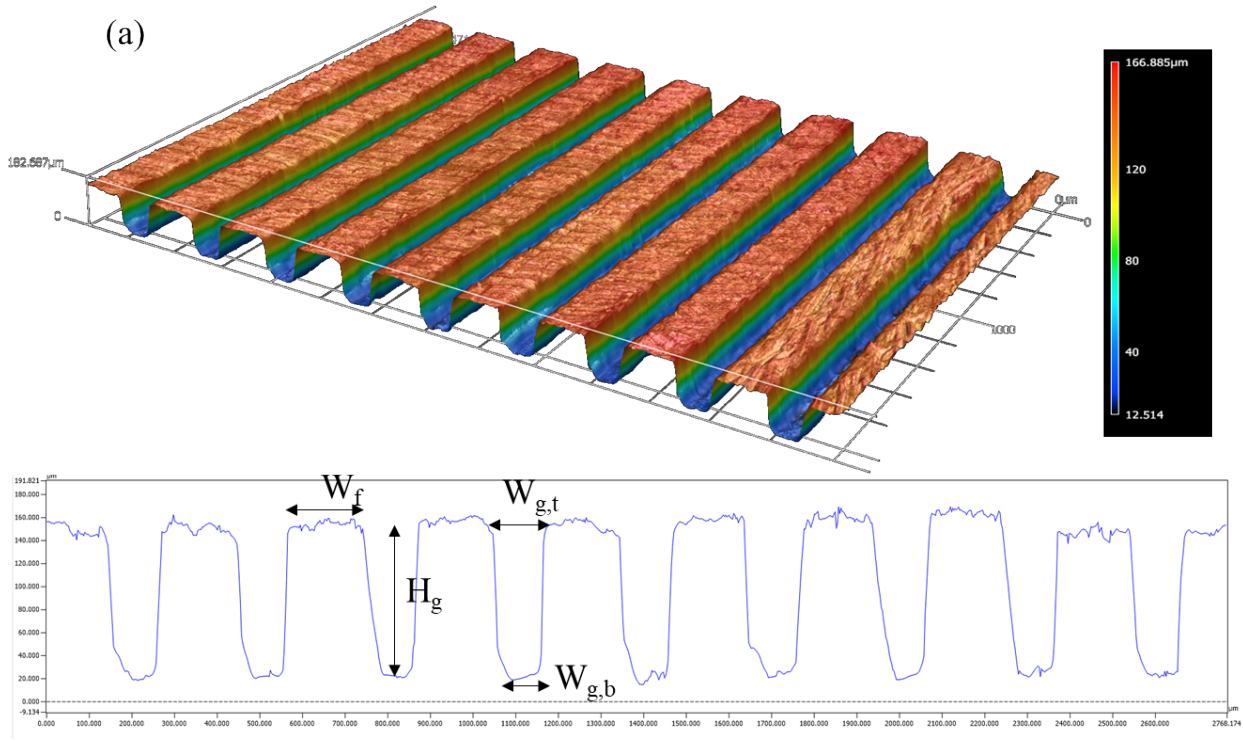

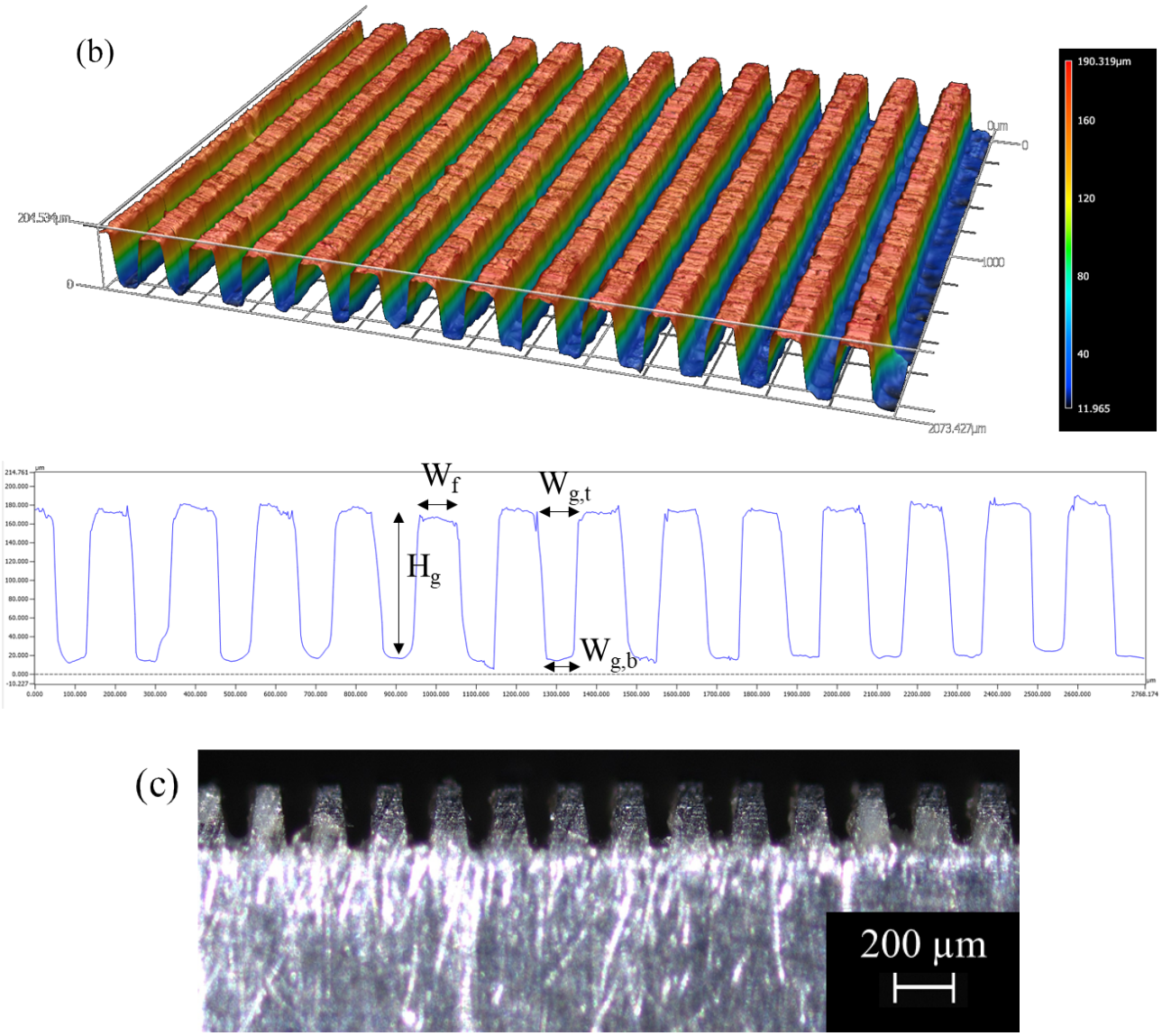

Fig. 3. Surface topography of the inverted trapezoid microgroove structures: (a) enhanced surface 1 (b) enhanced surface 2, and (c) microscopic view of the microgroove for enhanced surface 2.

Table 3: Dimensional details of the microgroove structures.

	Values	
Profile parameter	**Enhanced surface 1**	**Enhanced surface 2**
Fin width, W_f	173±3 µm	103±4 µm
Channel width at the top, $W_{g,t}$	126±4 µm	116±5 µm
Channel width at the bottom, $W_{g,b}$	64±4 µm	67±4 µm
Channel height, H_g	132±5 µm	160±3 µm

Prior to the pool boiling experiments, the pressure vessel was evacuated using a vacuum pump for three hours, and the vacuum condition was maintained overnight. After thoroughly inspecting the system, the liquid refrigerant was charged into the pressure vessel. Following the charging process, the 15-kW recirculating chiller was activated, and a solenoid valve was opened to supply cold water to the condenser. The chiller provided the necessary cooling power to the condenser. The saturation temperature of the refrigerant was maintained by controlling the vessel wall temperature, the inlet temperature of the cooling water, and the cooling water flow rate. Once the desired saturation conditions were achieved, the cartridge heaters in the heating block were turned on and set to the desired conditions. The heat flux was varied from 5 to 185 kW/m^2. Additionally, a Photron high-speed camera was placed next to the pressure vessel to record the boiling process, with videos captured at 1000 frames per second.

3. Data reduction

The heat input to the heating block is estimated using Fourier's law of heat conduction, as shown below:

$$q'' = -k\frac{dT}{dx} \tag{1}$$

where q'' is the heat flux (W m^{-2}), k represents the thermal conductivity of aluminum (Wm^{-1} K^{-1}), and $\frac{dT}{dx}$ denotes the temperature gradient along the heating block (K m^{-1}). The thermal conductivity of the aluminum block was measured using the hot disk method and was found to be 171.8 W m^{-1} K^{-1}, with an uncertainty of 3.26%. This study employs an aluminum heating block for the pool boiling tests due to its lower thermal conductivity compared to copper, which results in a larger temperature gradient along the heating block. This increased temperature difference helps minimize the uncertainty associated with the temperature gradient.

The temperature of the boiling surface (i.e., wall temperature) is estimated using the following expression:

$$T_{wall} = \max\{T_1, T_2, T_3\} - \frac{q''\delta}{k} \tag{2}$$

where T_{wall} represents the wall temperature (K), $T_1, T_2,$ and T_3 are the temperature measurements close to the top of the heating block (K), and δ is the vertical distance (i.e., 3.5 mm) between the thermocouples $\left(T_1, T_2, T_3\right)$ and the boiling surface (m).

The pool boiling heat transfer coefficient is calculated using the following relationship:

$$h = \frac{q''}{T_{wall} - T_{sat}} \tag{3}$$

where h is the pool boiling heat transfer coefficient (W m^{-2} K^{-1}) and T_{sat} represents the saturation temperature (K). The saturation temperature was measured using T-type thermocouples as described in Section 2.

The uncertainties (δU) of the heat flux and heat transfer coefficient are calculated using the error propagation method described in [25], and are defined as follows:

$$\delta U\left(Y_1, Y_2, ..., Y_N\right) = \sqrt{\sum_{j=1}^{N}\left(\frac{\partial U}{\partial Y_j}\delta Y_j\right)^2} \tag{4}$$

where δU is the uncertainty, $Y_1, Y_2, ..., Y_N$ are the independent parameters, and δY_j represents the uncertainty of each independent parameters. The maximum uncertainty of the HTC is estimated to be within 15%.

4. Results and Discussion

4.1 Validation of the experimental setup

The pool boiling experiments were conducted on a plain surface using R134a at a saturation temperature of 25℃ to validate the experimental setup. The heat transfer coefficients of R134a from this study is compared against the Rohsenow correlation [26] and updated Gorenflo Correlation [27], as shown in Fig. 4. Additionally, the HTCs from this study is compared with those from Moreno et al. [28] and Forrest et al. [29], as presented in Fig. 4. It is important to note that the HTCs from Moreno et al. [28] and Forrest et al. [29] were obtained under similar conditions to those of this study (i.e., R134a and T_{sat} = 25℃).

Fig. 4. Shows that the experimental data from this study align well with both the Rohsenow correlation [26] and Gorenflo correlation [27]. The maximum deviation between the experimental data and Rohsenow correlation [26] is nearly 10% and the same for Gorenflo correlation [27] is nearly 16%, which is within experimental uncertainties. Moreover, the HTCs of this study is similar to that of Moreno et al. [28] and Forrest et al. [29], validating the experimental setup. The Rohsenow correlation [26] is given by:

$$h = \frac{q''}{T_{wall} - T_{sat}} = \left(\frac{q''}{h_{fg}} \right)^{\frac{2}{3}} \left(\frac{g\left(\rho_l - \rho_v\right)}{\sigma} \right)^{\frac{1}{6}} \left(\frac{c_{p,l}\mu_l^{\frac{1}{3}}}{C_{s,l}\,\mathrm{Pr}^{1.7}} \right) \tag{5}$$

where $C_{s,l}$ represents the surface-liquid factor, accounting for boiling surface characteristics such as material and roughness, with a value of 0.0039 [29], h_{fg} is the latent heat of vaporization (kJ kg^{-1}), g denotes the acceleration due to gravity (m s^{-2}), σ indicates the surface tension (N m^{-1}), $c_{p,l}$ is the liquid specific heat (kJ kg^{-1} K^{-1}), μ_l is the dynamic viscosity (Pa s), Pr indicates Prandtl number, and ρ_l and ρ_v are the liquid and vapor density (kg m^{-3}), respectively.

Gorenflo correlation [27] is given by:

$$\frac{h}{h_{ref}} = \left(\frac{q''}{q''_{ref}} \right)^{0.95-0.3P^{*0.3}} \left(0.7P^{*0.2} + 4P^{*} + \frac{1.4P^{*}}{1-P^{*}} \right) \left(\frac{P_f}{P_{f,ref}} \right)^{0.6} \left(\frac{Ra}{Ra_{ref}} \right)^{2/15} \left(\frac{(k\rho c)_{Al}}{(k\rho c)_{Cu}} \right)^{0.25} \tag{6}$$

Where h_{ref} is 4.26 kW m^{-2} K^{-1}, q''_{ref} is 20 kW m^{-2}, P^{*} denotes the reduced pressure, $P_f = \dfrac{\left(\frac{dP}{dT}\right)}{\sigma}$ (μm^{-1} K^{-1}), $\frac{dP}{dT}$ is the slope of the vapor pressure curve (kPa K^{-1}), $P_{f,ref}$ is 1.333 μm^{-1} K^{-1}, Ra indicates the surface roughness value (μm), Ra_{ref} is 0.4 μm, and $(k\rho c)_{Al}$ and $(k\rho c)_{cu}$ are the effusivity of aluminum and copper (kW s$^{0.5}$ m^{2} K^{-1}), respectively.

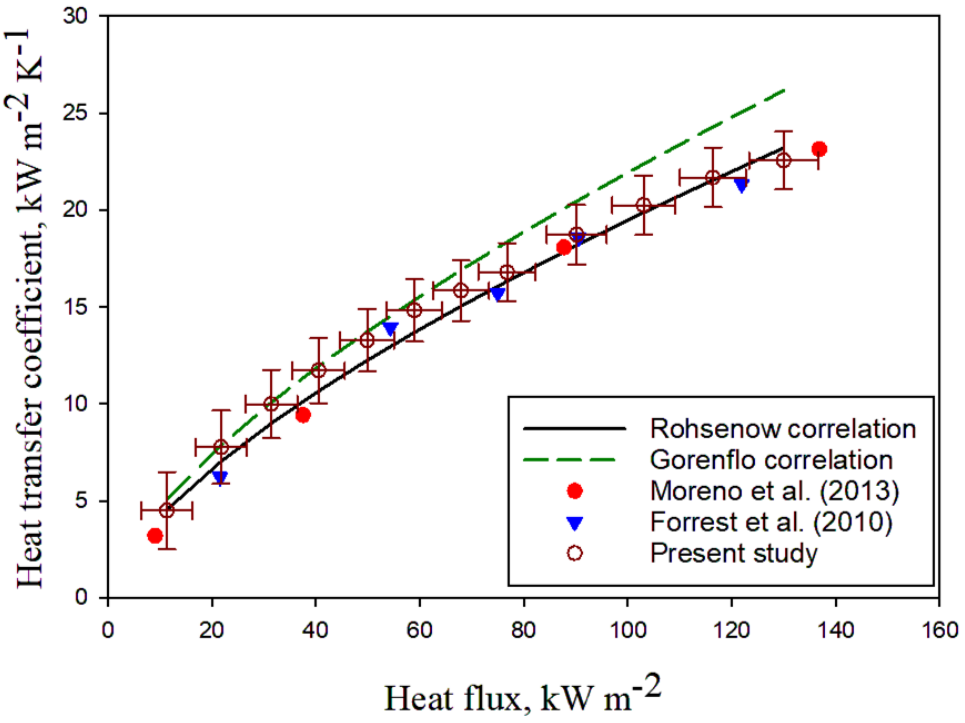

Fig. 4. Validation of the test setup against the Rohsenow correlation [26], Gorenflo correlation [27], and HTCs results from Moreno et al. [28] and Forrest et al. [29]. Note that HTCs results are for R134a at a saturation temperature of 25°C.

4.2 Performance of microgroove structures

As discussed in Section 2, two different enhanced surfaces were tested in this study, and their HTCs are compared with those of a plain surface, as shown in Fig. 5. The pool boiling characteristics of these surfaces are analyzed for R134a, R1234yf, and R1234ze(E), as presented in Figs. 5(a), (b), and (c), respectively. Overall, both the enhanced surfaces demonstrated higher HTCs compared to the plain surface. Specifically, enhanced surface 2 provided a maximum improvement of 80% over the plain surface, while enhanced surface 1 showed a 32%. Generally, enhanced surfaces have a larger surface area compared to plain surfaces. This increased surface area results in a greater number of nucleation sites, which aids in enhancing pool boiling heat transfer. This trend can be explained using Carey's boiling theory [30], as described below:

$$N_a = \left(r_c \left(\frac{h_{fg}\rho_v}{2\sigma T_{sat}} \Delta T \right) \right)^n \tag{6}$$

where N_a represents the number of active nucleation sites, r_c is the radius of cavities in the boiling surface (m), h_{fg} denotes the latent heat of vaporization (J kg^{-1}), ρ_v indicates the vapor density (kg m^{-3}), σ is the surface tension (N m^{-1}), n is an empirical constant, and T_{sat} and ΔT are the saturation temperature and wall superheat (K), respectively. According to Carey's boiling theory [30], the number of active nucleation sites on a boiling surface is influenced by the thermophysical properties of working fluid, wall superheat, saturation temperature (otherwise reduced pressure, which is a ratio of saturation pressure to critical pressure), and surface characteristics. From Fig. 6, it is observed that the enhanced surfaces have many tiny and rough cavities in the channels. These tiny and rough cavities act as nucleation sites, activating bubble nucleation [31]. In contrast, the plain surface is relatively smoother, with a roughness value of 1.052 µm. Consequently, the higher HTCs observed on the enhanced surfaces can be attributed to the increased number of nucleation sites and the larger surface area.

From Fig. 5, it is evident that enhanced surface 2 exhibits a higher HTC compared to enhanced surface 1. This indicates that, in addition to the increase in surface area, the microgroove profile also plays a crucial role in determining pool boiling HTC. Notably, channel width is almost identical for both the enhanced surfaces. However, the channel depth and fin width differ. The fin widths of enhanced surfaces 1 and 2 are 173 µm and 103 µm, respectively. The smaller fin width in enhanced surface 2 indicates more channels and higher surface area compared to the enhanced surface 1. As a result, the enhanced surface 2 provides higher HTC due to more nucleation sites caused by higher surface area. Besides the fin width, enhanced surface 1 has a channel depth of 132 µm, while enhanced surface 2 has a depth of 160 µm, as presented in Table. 3. The unique inverted trapezoid-shaped microgrooves can generate a capillary driving force, which ensures constant liquid replenishment to the boiling surface. The mass flowrate caused by capillary-driven mechanism can be estimated using the below relationships [32, 33]:

$$m_l = \frac{8\rho_l A_l^3}{K\mu_l L_{wet}^2 L_c}\left(\frac{2\sigma\cos\theta}{W}\right) \tag{7}$$

Where

$$K = \frac{8H_g^2}{\left(\frac{W}{2}\right)^2\left(1+\frac{2H_g}{W}\right)^2\left(\frac{1}{3}-\frac{32W}{\pi^5 H_g \tanh(\pi H_g/W)}\right)} \tag{8}$$

Where m_l is the mass flowrate caused by capillary driven mechanism (kg m s^{-1}), ρ_l indicates the liquid density (kg m^{-3}), A_l represents the cross-sectional area of the channel (m^2), σ denotes the surface tension (N m^{-1}), μ_l is the viscosity (Pa s), L_w means the wetted perimeter of a channel (m), L_c is the length of the capillary pumping region (m), W is the channel width, and K is the Darcy-Weisbach friction coefficient.

The mass flow rates estimated, for R134a at a saturation temperature of 15°C, for enhanced surface 1 and enhanced surface 2 are 8.27×10^{-9} kg m^{-1} s^{-1} and 1.14×10^{-8} kg m^{-1} s^{-1}, respectively. The mass flow induced by capillary-assisted wicking mechanism is almost one order of magnitude higher in enhanced surface 2 compared with enhanced surface 1. Based on this, it is clear that the deeper channels in enhanced surface 2 provides greater capillary-assisted wicking than enhanced surface 1, delivering more liquid to the microgrooves through capillary action and enhancing microlayer evaporation. Consequently, enhanced surface 2 offers a higher HTC than enhanced surface 1 due to increased capillary-assisted liquid feeding. Similarly, Kwak et al. [32] also found that, for a fixed channel width, the heat transfer coefficient increases with channel height due to the increased capillary assisted wicking.

According to Fig. 5, the HTCs of the enhanced surfaces are similar to those of the plain surface up to a heat flux of ~45 kW m^{-2}. However, for heat fluxes greater than ~45 kW m^{-2}, the HTCs of the enhanced surfaces gradually increase compared to the plain surface, with the percentage enhancement also rising with heat flux. Kwak et al. [32] observed similar behavior for pool boiling of water in microchannels. This behavior can be explained through bubble dynamics. Bubble dynamics of the plain and enhanced surfaces can be divided into two main regimes: (1) the isolated bubble regime and (2) the coalesced bubble regime. Ishibashi and Nisikawa [34] experimentally analyzed the characteristics of the isolated and coalesced bubble regions under saturated boiling in narrow spaces. Based on their experimental prediction, it is observed that HTC increases tremendously, as the spacing reduced, for a given heat flux in the coalesced bubble region compared to the isolated bubble region. In other words, the increase in HTC in the isolated bubble regime is marginal or negligible compared to coalesced bubble regime. Similarly, Kwak et al. [32] also found that the enhancement in HTC for microchannels is higher in coalesced bubble region compared to the isolated bubble region. Based on these characteristics described for isolated and

coalesced bubble regions, the present study identifies that isolated bubble region dominates for the heat fluxes less than ~45 kW m^{-2}.

In the isolated bubble regime, the bubble life cycle involves bubble nucleation, growth, and departure. In this regime, bubble embryos nucleate at the nucleation sites, and they will grow over time. Once they reach their maximum size, the bubbles depart from the boiling surface. During this cycle, coalescence with neighboring bubbles is minimal, as presented in Fig. 7. It can be seen from Figs. 7 (a)–(c) that the size of the bubbles is relatively smaller in the isolated bubble regime due to the minimal coalescence between neighboring bubbles at lower heat fluxes (i.e., within ~45 kW m^{-2}). The videos featuring pool boiling behavior of at two different heat fluxes of 26 kW m^{-2} and 181 kW m^{-2} for the enhanced surface 1 at a saturation temperature of 35°C are provided in the supplementary file. As a result, the isolated bubble regime may not encounter local dry spots, indicating that sufficient liquid is present on the boiling surface to sustain boiling, regardless of whether the surface is plain or enhanced. Consequently, the HTCs for both plain and enhanced surfaces are quite similar up to a heat flux of ~45 kW m^{-2}.

In the coalesced bubble regime, the bubble life cycle includes bubble nucleation, growth, coalescence, and departure. Coalescence is an additional stage in the bubble life cycle in this regime, compared to the isolated bubble regime. At high heat fluxes, a large number of nucleation sites become active due to higher wall superheat. As a result, bubbles from neighboring nucleation sites coalesce, as presented in Figs. 7 (d)–(f). It is apparent from Figs. 7 (d)–(f) that the bubble size is relatively larger at high heat fluxes (i.e., greater than ~45 kW m^{-2}). The formation larger bubbles due to coalescence can create a local vapor blanket (dry spots) on the boiling surface. The vapor blanket hinders the liquid supply to the boiling surface, disrupting the pool boiling process and reducing the HTC. For the plain surface, liquid replenishment is primarily driven by gravity-assisted pressure head $\left(\rho_l g h_v\right)$, where ρ_l is the liquid density (kg m^{-3}), g is the acceleration due to gravity (m s^{-2}), and h_v indicates the bubble height (m). For enhanced surfaces, liquid feeding is enabled by both gravity-assisted pressure head and capillary-assisted wicking. This combined effect accelerates liquid feeding to the microgrooves (i.e., boiling surface), a mechanism that is lacking in the plain surface. Due to the continuous liquid replenishment in the enhanced surfaces, the formation of local dry spots can be prevented. As a result, the HTCs of the enhanced surfaces

are significantly higher than those of the plain surface in the coalesced bubble regime (i.e., heat fluxes greater than ~45 kW m^{-2}).

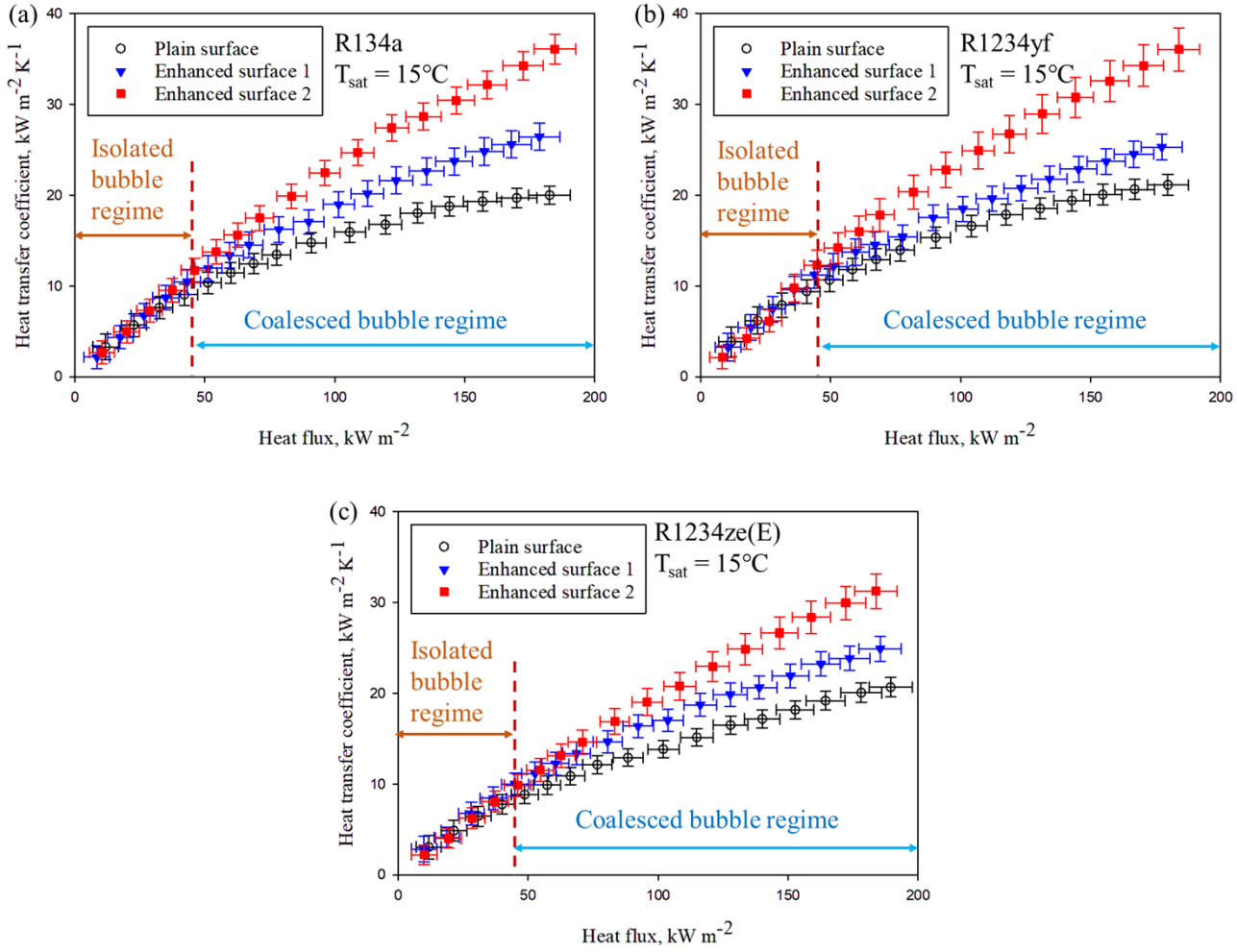

Fig. 5. Comparison of pool boiling HTCs of enhanced surfaces with plain surface for different refrigerants at a saturation temperature of 15°C: (a) R134a (b) R1234yf, and (c) R1234ze(E).

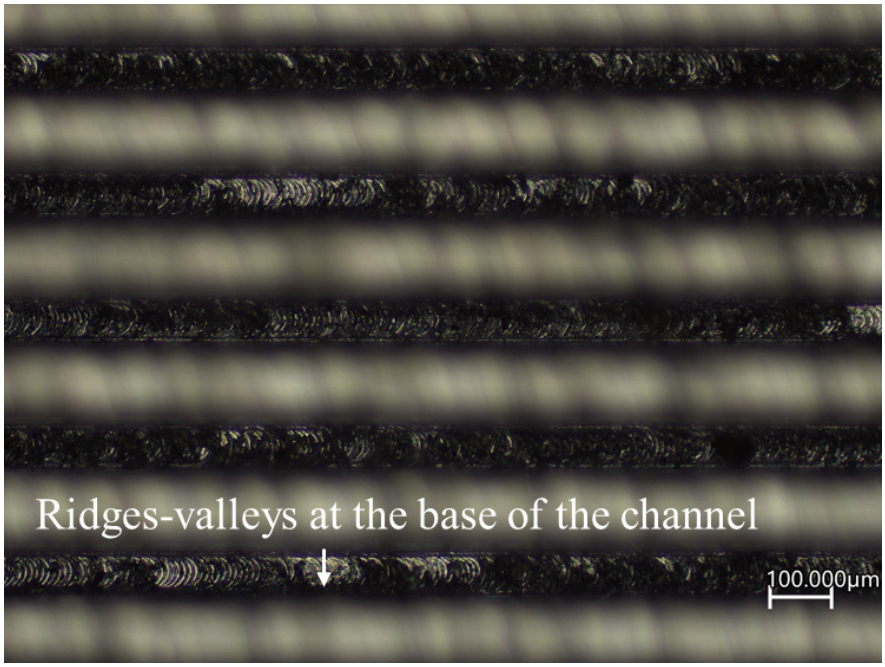

Fig. 6. Microscopic images featuring the surface characteristics of enhanced surface 2.

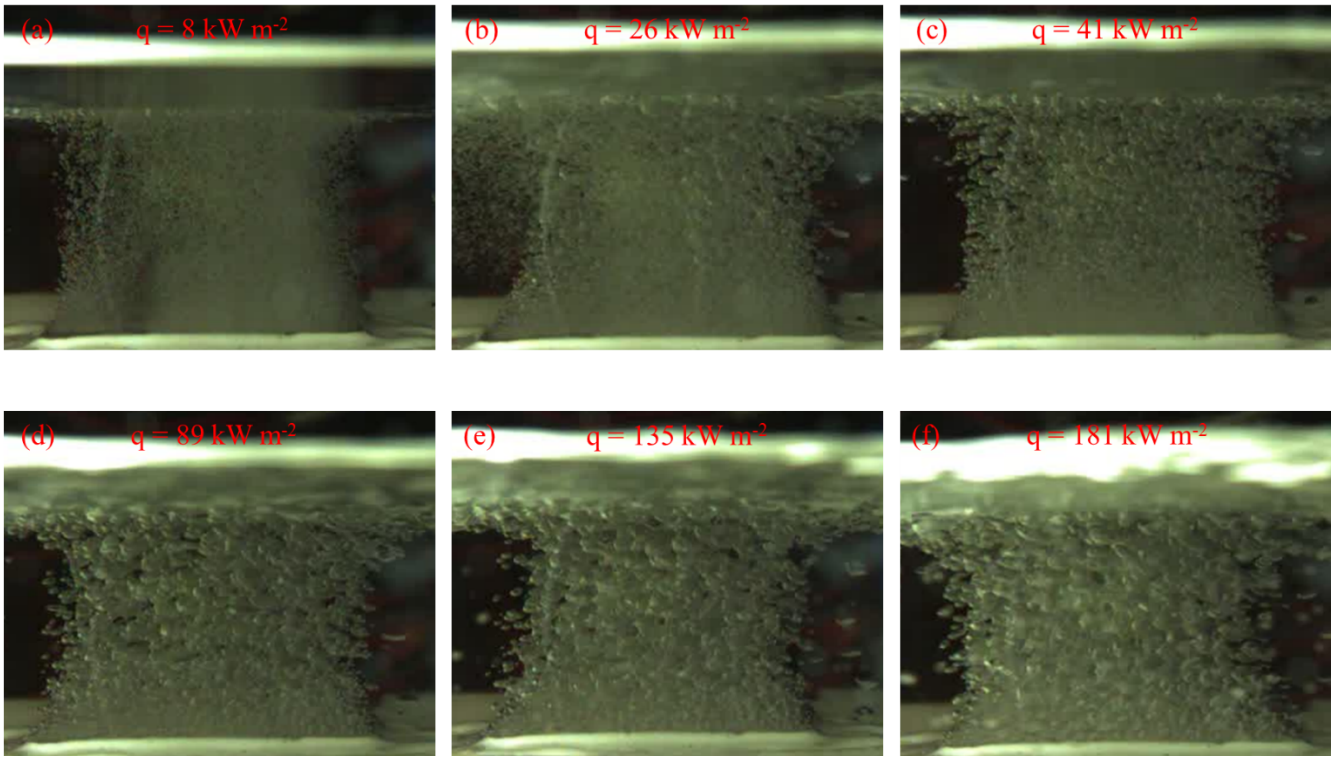

Fig. 7. Pool boiling behavior of R134a on enhanced surface 1 at a saturation temperature of 15°C: (a)–(c) depict the isolated bubble regime, characterized by minimal bubble coalescence and smaller bubble size at heat fluxes below ~45 kW m^{-2} and (d)–(f) illustrate the coalesced bubble regime, where increased coalescence with neighboring bubbles results in larger bubble sizes at heat fluxes exceeding ~45 kW m^{-2}.

4.3 Performance of R1234yf and R1234ze(E)

This study examines the pool boiling characteristics of HFO refrigerants R1234yf and R1234ze(E), comparing their performance with R134a. The analysis is conducted on both plain and enhanced surfaces, as presented in Figs. 8–10. Additionally, the study investigates the effect of saturation temperatures on the pool boiling HTCs of R134a, R1234yf, and R1234ze(E).

From Figs. 8–10, it is observed that the pool boiling HTCs of R1234yf are similar to those of R134a across the saturation temperature range of 15–35°C for both plain and enhanced surfaces. The thermophysical properties of these refrigerants significantly influence their pool boiling HTCs. Key thermophysical properties of R134a, R1234ze(E), and R1234yf are listed in Table 4. Notably, the latent heat of vaporization for R134a is nearly 18% higher than that of R1234yf. Despite this lower latent heat, the HTCs of R1234yf are similar to those of R134a. Pool boiling HTCs depend on various thermophysical properties and reduced pressures, in addition to latent heat. Particularly, density and surface tension of the refrigerant play a critical role in wetting characteristics and bubble departure behavior. For instance, the surface tension of R1234yf is nearly 22% lower than that of R134a. Lower surface tension enhances wettability, which is beneficial for pool boiling.

Saini et al. [35] investigated how the Jakob number ($Ja = \frac{c_{p,l}\rho_l\left(T_{wall} - T_{sat}\right)}{\rho_v h_{fg}}$), which represents the ratio of sensible heat to latent heat during phase change process, affects bubble departure under pool boiling conditions. They assessed the roles of various forces, including surface tension, buoyancy, inertial force, and viscous drag, in the process of bubble departure under pool boiling conditions. Their force balance model indicates that when $\log(Ja) < 1.2$, surface tension governs bubble growth and departure. Conversely, when $\log(Ja) > 2.0$, inertial forces take over. In this study, the estimated $\log(Ja)$ for the observed range of wall superheats is less than 1.2, suggesting

that surface tension plays a more significant role than inertial forces in influencing the bubble growth and departure cycle. Therefore, the bubble departure diameter is calculated using the Fritz model, which accounts for the effects of surface tension, enhancing our comprehension of bubble departure behavior. Fritz [36] derived a relationship for bubble departure diameter as a function of density and surface tension, presented in Eqn. 7.

$$D_b = 0.02058\beta\sqrt{\frac{\sigma}{g\left(\rho_l - \rho_v\right)}} \tag{9}$$

where D_b is the bubble departure diameter (m), σ represents the surface tension of the liquid (N m^{-1}), g is the gravitational acceleration (m s^{-2}), ρ_l indicates the liquid density (kg m^{-3}), ρ_v denotes the vapor density (kg m^{-3}), and $\beta = 35°$ for refrigerants. The estimated bubble departure diameter at T_{sat} = 15°C is 0.608 mm for R1234yf and 0.647 mm for R134a, indicating that R1234yf has a bubble departure diameter nearly 6% smaller than that of R134a. A smaller bubble departure diameter allows bubbles to leave the surface more quickly, enhancing pool boiling heat transfer. Additionally, the reduced pressure, ratio of saturation pressure to critical pressure, plays a significant role in influencing pool boiling HTC. The higher the reduced pressure, the better the pool boiling HTC. From Table 4, the reduced pressure for R1234yf is nearly 20% higher than that of R134a at a given saturation temperature. In summary, the higher reduced pressure (20%) and smaller bubble departure diameter (6%) are more favorable for R1234yf compared with R134a, which likely compensates for the lower latent heat of vaporization of R1234yf. Consequently, the HTCs of R1234yf are similar to those of R134a.

In contrast to R1234yf, pool boiling HTCs of R1234ze(E) are slightly lower than those of R134a. The reduction in HTCs for R1234ze(E) can be attributed to its thermophysical properties and reduced pressures. The latent heat of vaporization of R1234ze(E) is nearly 7% lower than that of R134a. Additionally, the bubble departure diameter of R1234ze(E) is 0.69 mm at T_{sat} = 15°C, which is about 7% larger than that of R134a. Moreover, the reduced pressure of R1234ze(E) is 17% lower than that of R134a. Overall, the lower latent heat of vaporization, lower reduced pressure, and larger bubble departure diameter compared to R134a may contribute to the reduced pool boiling HTCs for R1234ze(E).

This study also investigates the influence of saturation temperature on both plain and enhanced surfaces, as presented in Figs. 8–10. The pool boiling HTCs increase with saturation temperature, regardless of the refrigerants and surface types. This increase in HTC with saturation temperature is mainly attributed to the rise in reduced pressure with saturation temperature. The reduced pressures of R134a, R1234ze(E), and R1234yf are listed in Table 5for saturation temperatures of 15℃, 25℃, and 35℃. For R134a, R1234ze(E), and R1234yf, the reduced pressure increases by approximately 3–3.6% for every 1℃ rise in saturation temperature. As the pressure increases, the number of active nucleation sites also increases. Furthermore, at high saturation pressures (i.e., high saturation temperatures), the bubble departure diameter decreases due to the reduction in surface tension. The combined effect of a greater number of nucleation sites and smaller bubble departure diameters likely contributes to the rise in pool boiling HTCs at higher saturation temperatures. Similar trends of increased pool boiling HTC with rising saturation temperature due to increased reduced pressure have been reported by Shah et al. [37], Kumar and Wang [24], and Dahariya and Betz [38]. Moreover, comparing Figs. 8 – 10, it is noted that the HTC enhancement ratio (ratio of microgroove structure HTC to plain surface HTC) remained identical for each refrigerant tested in this study

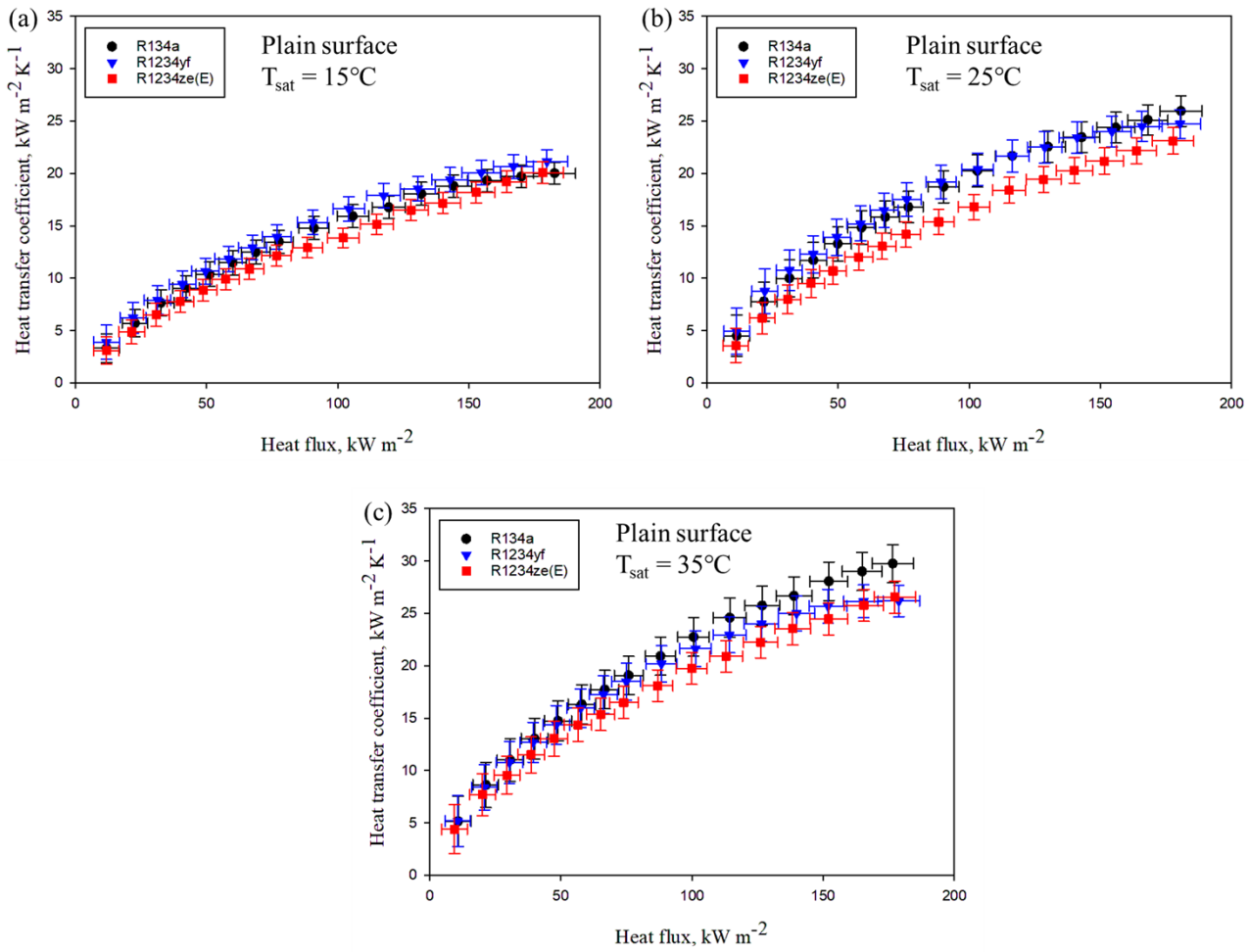

Fig. 8. Comparison of pool boiling HTCs of R1234yf and R1234ze(E) with R134a for plain surface: (a) T_{sat} = 15°C, (b) T_{sat} = 25°C, and (c) T_{sat} = 35°C.

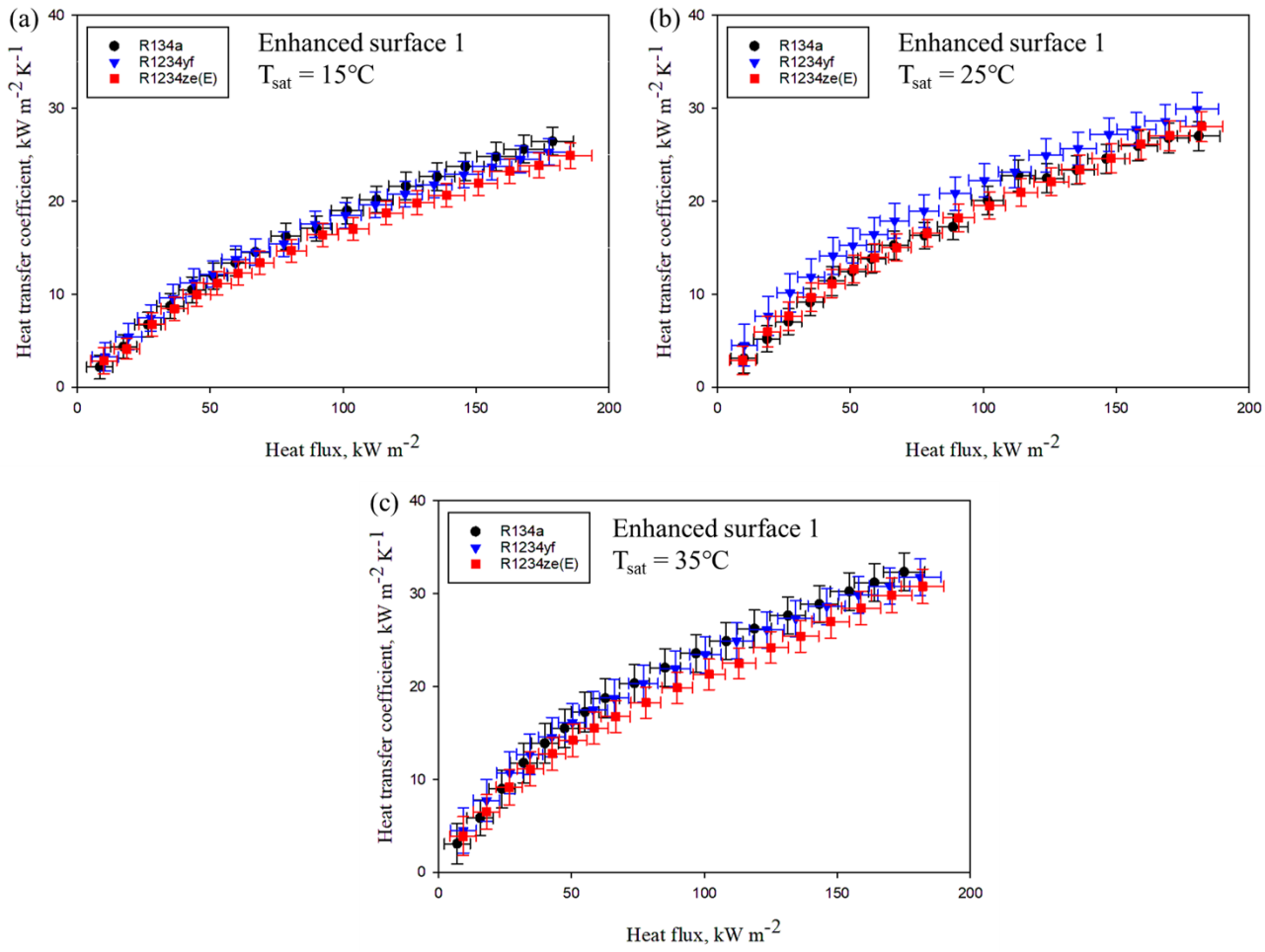

Fig. 9. Comparison of pool boiling HTCs of R1234yf and R1234ze(E) with R134a for enhanced surface 1: (a) T_{sat} = 15°C, (b) T_{sat} = 25°C, and (c) T_{sat} = 35°C.

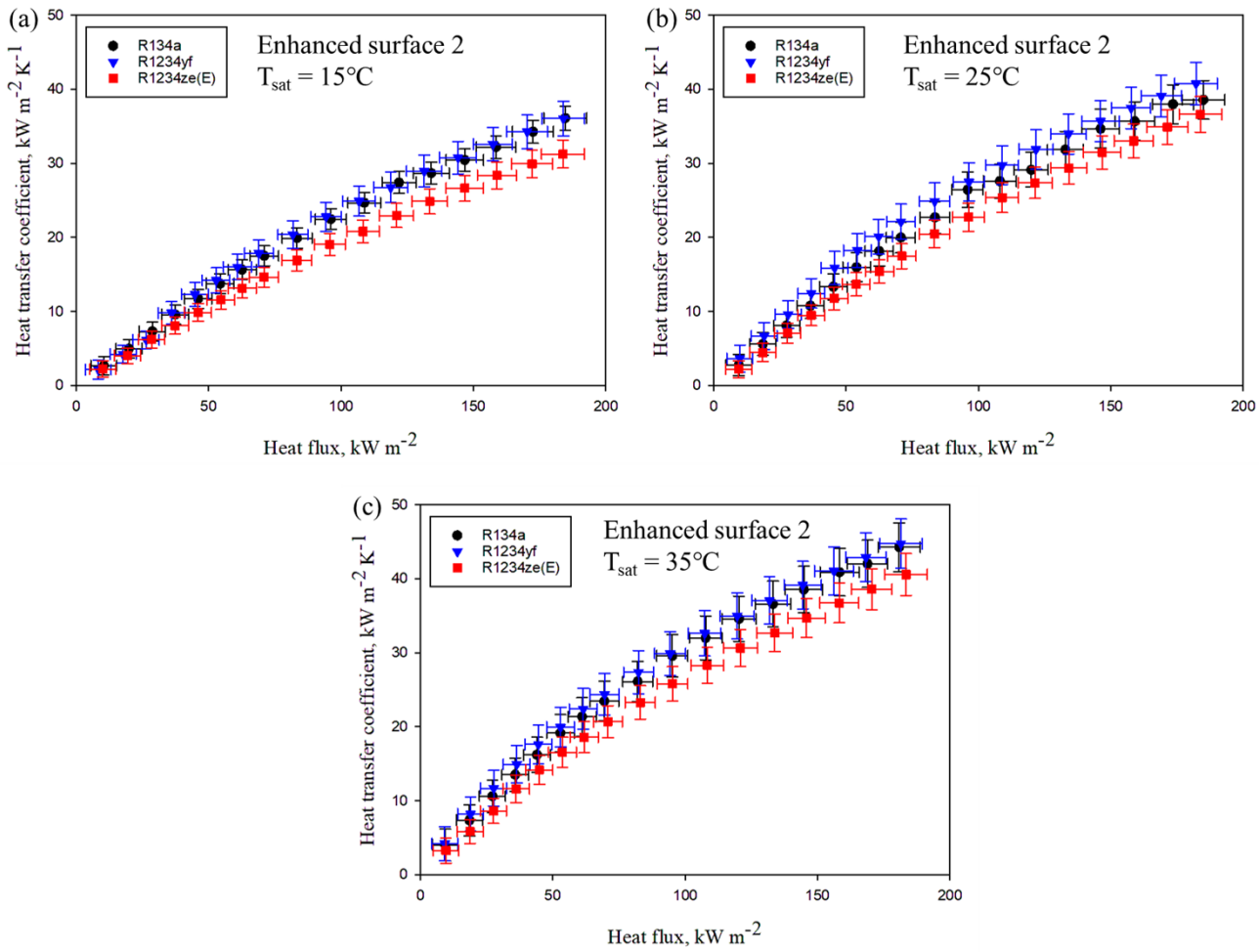

Fig. 10. Comparison of pool boiling HTCs of R1234yf and R1234ze(E) with R134a for enhanced surface 2: (a) T_{sat} = 15°C, (b) T_{sat} = 25°C, and (c) T_{sat} = 35°C.

Table 4: Thermophysical properties of R134a, R1234yf, and R1234Ze(E) at a saturation temperature of 15℃.

Properties	**R-134a**	**R-1234ze(E)**	**R-1234yf**
Saturation pressure, kPa	488.7	366	510.2
Critical pressure, kPa	4059	3632	3382
Reduced pressure	0.12	0.10	0.15
Molar mass, kg $kmol^{-1}$	102	114	114
Liquid density, kg m^{-3}	1243	1195	1127
Vapor density, kg m^{-3}	23.78	19.63	28.32
Latent heat, kJ kg^{-1}	186.6	174	153
Surface tension, N m^{-1}	0.009	0.01	0.007
Liquid viscosity, Pa s	2.20E-04	2.10E-04	1.70E-04
Vapor viscosity, Pa s	1.10E-05	1.10E-05	1.00E-05
Liquid thermal conductivity, W m^{-1} K^{-1}	0.087	0.078	0.066
Vapor thermal conductivity, W m^{-1} K^{-1}	0.013	0.013	0.013
Liquid specific heat, kJ kg^{-1} K^{-1}	1.38	1.37	1.34

Table 5: Reduced pressure details of R134a, R1234ze(E), and R1234yf at different saturation temperatures.

Parameters	**R134a**			**R1234ze(E)**			**R1234yf**		
Saturation temperature, ℃	15	25	35	15	25	35	15	25	35
Saturation pressure, kPa	488.7	665.8	887.5	366	500.1	668.5	510.2	682.5	895.2
Critical pressure, kPa		4059			3632			3382	
Reduced pressure	0.12	0.16	0.22	0.10	0.14	0.18	0.15	0.20	0.26

5. Conclusions

This study investigates the pool boiling heat transfer characteristics of novel inverted trapezoid microgroove structures using HFO refrigerants. The performance of two different microgroove structures is compared with that of plain surface. Moreover, the pool boiling HTCs of R1234yf, R1234ze(E) are compared against those of R134a. Additionally, the influence of saturation temperature on pool boiling HTCs is also examined for both microgroove and plain surfaces at different saturation temperatures of 15℃, 25℃, and 35℃. The experimental results demonstrated that the enhanced surface 2 can provide a maximum of 80% increase in pool boiling HTCs compared to those of plain surface, while the enhanced surface 1 provided enhancement up to 32%. And the performance of microgroove structures is comparable to that of plain surface up to a heat flux of 45 kW m^{-2} due to isolated bubble regime. Whereas, for the heat fluxes greater than 45 kW m^{-2}, the HTCs of enhanced surfaces are gradually increased compared to those of the plain surface.

Conflict of interest

None.

Acknowledgement

The authors would like to express their sincere gratitude to the U.S. Department of Energy – Building Technologies Office, along with technology managers Mr. Antonio Bouza and Dr. Payam Delgoshaei, for their invaluable support. We also extend our heartfelt thanks to the Building Technologies Research and Integration Center, as well as Tim Dyer, Charles Pierce, Chavez Chelo, Douglas Stringfield, Brent Massey, Anthony Gehl, Brian Goins, and Joshua Standifier for their exceptional technical assistance.

References

[1] https://ww2.arb.ca.gov/resources/documents/high-gwp-refrigerants

[2] A. K. Dewangan, S. K. Sajjan, A. Kumar, and R. Kumar, "Pool boiling heat transfer on a plain tube in saturated R-134a and R-410A," *Heat and Mass Transfer,* vol. 56, no. 4, pp. 1179-1188, 2020.

[3] C.-Y. Hsu, L.-H. Chien, and J.-C. Chang, "Experimental study of falling film evaporation of refrigerants, R32, R1234yf, R410A, R452B and R454B on horizontal tubes," *International Journal of Heat and Mass Transfer,* vol. 205, p. 123914, 2023.

[4] J. Li, L. Lin, S. Li, Z. Yang, and Y. Duan, "Experimental study on nucleate pool boiling heat transfer characteristics of R32+ R1234yf binary mixtures," *Applied Thermal Engineering,* vol. 205, p. 118047, 2022.

[5] D. Jung, Y. Kim, Y. Ko, and K. Song, "Nucleate boiling heat transfer coefficients of pure halogenated refrigerants," *International Journal of Refrigeration,* vol. 26, no. 2, pp. 240-248, 2003.

[6] R. Köster, G. Herres, P. Kaupmann, and P. Hübner, "Influence of the heat flux in mixture boiling: experiments and correlations," *International journal of refrigeration,* vol. 20, no. 8, pp. 598-605, 1997.

[7] G. Ribatski and J. R. Thome, "Nucleate boiling heat transfer of R134a on enhanced tubes," *Applied Thermal Engineering,* vol. 26, no. 10, pp. 1018-1031, 2006.

[8] A. K. Dewangan, A. Kumar, and R. Kumar, "Experimental study of nucleate pool boiling of R-134a and R-410A on a porous surface," *Heat Transfer Engineering,* vol. 40, no. 15, pp. 1249-1258, 2019.

[9] M. Saidi, M. Ohadi, and M. Souhar, "Enhanced pool boiling of R-123 refrigerant on two selected tubes," *Applied thermal engineering,* vol. 19, no. 8, pp. 885-895, 1999.

[10] S.-S. Hsieh and C.-G. Ke, "Bubble dynamic parameters and pool boiling heat transfer on plasma coated tubes in saturated R-134a and R-600a," *J. Heat Transfer,* vol. 124, no. 4, pp. 704-716, 2002.

[11] M. Kedzierski and L. Lin, "Pool Boiling of R514A, R1224 yd (Z), and R1336mzz (E) on a Reentrant Cavity Surface," *Journal of Heat Transfer,* vol. 143, no. 5, p. 051602, 2021.

[12] M. A. Kedzierski and L. Lin, "Pool boiling of HFO-1336mzz (Z) on a reentrant cavity surface," *International Journal of Refrigeration,* vol. 104, pp. 476-483, 2019.

[13] M. A. Kedzierski, L. Lin, and D. Kang, "Pool Boiling of Low-Global Warming Potential Replacements for R134a on a Reentrant Cavity Surface," *Journal of Heat Transfer,* vol. 140, no. 12, 2018, doi: 10.1115/1.4040783.

[14] E. Gorgy, "Nucleate boiling of low GWP refrigerants on highly enhanced tube surface," *International Journal of Heat and Mass Transfer,* vol. 96, pp. 660-666, 2016/05/01/ 2016, doi: https://doi.org/10.1016/j.ijheatmasstransfer.2016.01.057.

[15] L. Lin and M. A. Kedzierski, "Review of low-GWP refrigerant pool boiling heat transfer on enhanced surfaces," *International journal of heat and mass transfer,* vol. 131, pp. 1279-1303, 2019.

[16] Y. Lee, D.-G. Kang, J.-H. Kim, and D. Jung, "Nucleate boiling heat transfer coefficients of HFO1234yf on various enhanced surfaces," *International journal of refrigeration,* vol. 38, pp. 198-205, 2014.

[17] E. van Rooyen and J. R. Thome, "Pool boiling data and prediction method for enhanced boiling tubes with R-134a, R-236fa and R-1234ze(E)," *International Journal of Refrigeration,* vol. 36, no. 2, pp. 447-455, 2013/03/01/ 2013, doi: https://doi.org/10.1016/j.ijrefrig.2012.11.023.

[18] K.-J. Park and D. Jung, "Nucleate boiling heat transfer coefficients of R1234yf on plain and low fin surfaces," *International Journal of refrigeration,* vol. 33, no. 3, pp. 553-557, 2010.

[19] R. Nagata, C. Kondou, and S. Koyama, "Enhancement of R1234ze(Z) pool boiling heat transfer on horizontal titanium tubes for high-temperature heat pumps," *Science and Technology for the Built*

Environment, vol. 23, no. 6, pp. 923-932, 2017/08/18 2017, doi: 10.1080/23744731.2017.1325706.

[20] H.-W. Byun, D. H. Kim, S. H. Yoon, C. H. Song, K. H. Lee, and O. J. Kim, "Pool boiling performance of enhanced tubes on low GWP refrigerants," *Applied Thermal Engineering,* vol. 123, pp. 791-798, 2017.

[21] M. A. Kedzierski, L. Lin, and D. Kang, "Pool boiling of low-global warming potential replacements for R134a on a reentrant cavity surface," *Journal of heat transfer,* vol. 140, no. 12, p. 121502, 2018.

[22] Y. Lee, D. G. Kang, H. Seo, and D. Jung, "Pool boiling heat transfer coefficients of R1234yf on various enhanced surfaces," *Korean Journal of Air-Conditioning and Refrigeration Engineering,* vol. 25, no. 3, pp. 143-149, 2013.

[23] E. Van Rooyen and J. Thome, "Pool boiling data and prediction method for enhanced boiling tubes with R-134a, R-236fa and R-1234ze (E)," *International journal of refrigeration,* vol. 36, no. 2, pp. 447-455, 2013.

[24] A. Kumar and C.-C. Wang, "Nucleate pool boiling heat transfer of R-1234ze (E) and R-134a on GEWA-B5H and smooth tube with the influence of POE oil," *Applied Thermal Engineering,* vol. 201, p. 117779, 2022.

[25] R. J. Moffat, "Describing the uncertainties in experimental results," *Experimental thermal and fluid science,* vol. 1, no. 1, pp. 3-17, 1988.

[26] W. M. Rohsenow, "A method of correlating heat-transfer data for surface boiling of liquids," *Transactions of the American Society of Mechanical Engineers,* vol. 74, no. 6, pp. 969-975, 1952.

[27] P. Stephan and V. H. Atlas, "B1 Fundamentals of Heat Transfer'," *VDI Heat Atlas,* pp. 15-30, 2010.

[28] G. Moreno, S. Narumanchi, and C. King, "Pool boiling heat transfer characteristics of HFO-1234yf on plain and microporous-enhanced surfaces," *Journal of heat transfer,* vol. 135, no. 11, p. 111014, 2013.

[29] E. C. Forrest, L.-W. Hu, T. J. McKrell, J. Buongiorno, and Y. Ostrovsky, "Pressure Effects on the Pool Boiling of the Fluorinated Ketone c 2 f 5 c (o) cf (cf 3) 2," in *2010 12th IEEE Intersociety Conference on Thermal and Thermomechanical Phenomena in Electronic Systems*, 2010: IEEE, pp. 1-9.

[30] V. P. Carey, *Liquid-vapor phase-change phenomena: an introduction to the thermophysics of vaporization and condensation processes in heat transfer equipment*. CRC Press, 2020.

[31] G. Pi, D. Deng, L. Chen, X. Xu, and C. Zhao, "Pool boiling performance of 3D-printed reentrant microchannels structures," *International Journal of Heat and Mass Transfer,* vol. 156, p. 119920, 2020.

[32] H. J. Kwak, J. H. Kim, B.-S. Myung, M. H. Kim, and D. E. Kim, "Behavior of pool boiling heat transfer and critical heat flux on high aspect-ratio microchannels," *International Journal of Thermal Sciences,* vol. 125, pp. 111-120, 2018.

[33] G. Schneider, "Non-dimensional analysis for the heat transport capability of axially grooved heat pipes including liquid/vapor interaction," in *18th aerospace sciences meeting*, 1980, p. 214.

[34] E. Ishibashi and K. Nishikawa, "Saturated boiling heat transfer in narrow spaces," *International Journal of Heat and Mass Transfer,* vol. 12, no. 8, pp. 863-893, 1969.

[35] J. Saini, C. Gupta, and S. Lal, "Effect of Jakob number on forces controlling bubble departure in nucleate pool boiling," *International Journal of Heat and Mass Transfer,* vol. 18, no. 3, pp. 472-474, 1975.

[36] W. Fritz, "Berechnung des maximalvolumes von dampfblasen," *Physik. Zeitschr,* vol. 36, pp. 379-384, 1935.

[37] B. A. Shah, P. Patel, and V. J. Lakhera, "Evaluation of Pressure, Surface Characteristics, and Fluid Properties Effect on Pool Boiling Heat Transfer Over Plain and External Micro-Finned Cylindrical

Surfaces," *Journal of Thermal Science and Engineering Applications,* vol. 15, no. 11, p. 111011, 2023.

[38] S. Dahariya and A. R. Betz, "High pressure pool boiling: Mechanisms for heat transfer enhancement and comparison to existing models," *International Journal of Heat and Mass Transfer,* vol. 141, pp. 696-706, 2019.